Modeling of Light Scattering from Structures with Particle Contaminants

Brent M. Nebeker, Greg W. Starr, and E. Dan Hirleman

Arizona State University, Department of Mechanical and Aerospace Engineering,
Box 876106, Tempe, AZ 85287-6106

ABSTRACT

Detection of particle contaminants on patterned wafers is important for increasing yield during the silicon wafer manufacturing process. Surface scanning inspection systems are used to detect contamination by measuring scattering from coherent light incident on the wafer surfaces. To aid in the design of these inspection systems, a code based on the coupled-dipole method has been developed to predict scattering from features on surfaces. To validate the code, we show comparisons between experimental results and numerical predictions of scattering characteristics of patterned structures found on the Arizona State University/Semiconductor Research Corporation block of the SEMATECH patterned wafer defect standard die developed by VLSI Standards, Inc.. The patterned structures considered here are SiO_2 line features and cornered features on silicon substrates. Particle contamination is emulated with deposition of PSL spheres near these structures. Comparisons of the differential scattering cross-section are made between experiment and the computational results. Close agreement within a factor of 2 to 3 is found for the cases considered.

Keywords: light scattering, coupled-dipole method, discrete-dipole approximation, surface features, differential scattering cross-section, optical inspection

1. INTRODUCTION

Detection and characterization of features on wafer surfaces by optical wafer inspection systems are an important consideration in the semiconductor industry. These inspection systems measure scattered light from coherent light sources incident on the wafer. Because of the broad range of particles, defects, and substrates that exist in the semiconductor industry, a numerical scattering model could provide a more efficient means of system calibration as compared to experimental calibration. In this paper, a method to model light scattering from features on surfaces is described, and comparisons with experimental results are made. The model uses the coupled-dipole method, also known as the discrete-dipole approximation (DDA). In the coupled-dipole method, dipoles are positioned in lattice sites to model a feature shape. The dipole properties model the feature composition. An electric field from an incident light source induces a dipole moment at each dipole. Once the moment at each dipole is determined, the scattered field outside the particle boundary can be determined. The coupled-dipole method was originally developed to model particles in free space.[1,2,3] The method was modified to model particles on surfaces by Taubenblatt and Tran[4] by employing the Sommerfeld integrals for interaction between dipoles and a surface. The code developed at Arizona State University called DDSURF[5] is based on the DDSCAT code for features in free space[3] with modifications to include surface interaction and employs a two-dimensional fast Fourier transform routine to accelerate solution time.[5]

In this paper, DDSURF is used to model light scattering from SiO_2 patterned features present within the Arizona State University/Semiconductor Research Corporation block of the SEMATECH patterned wafer defect standard die. PSL spheres were deposited on the patterned wafer to act as particle contamination. An overhead view of the three geometric configurations and contaminant positions considered here are shown in Figures 1a-c. The orientations of the incident beam on the features are also shown.
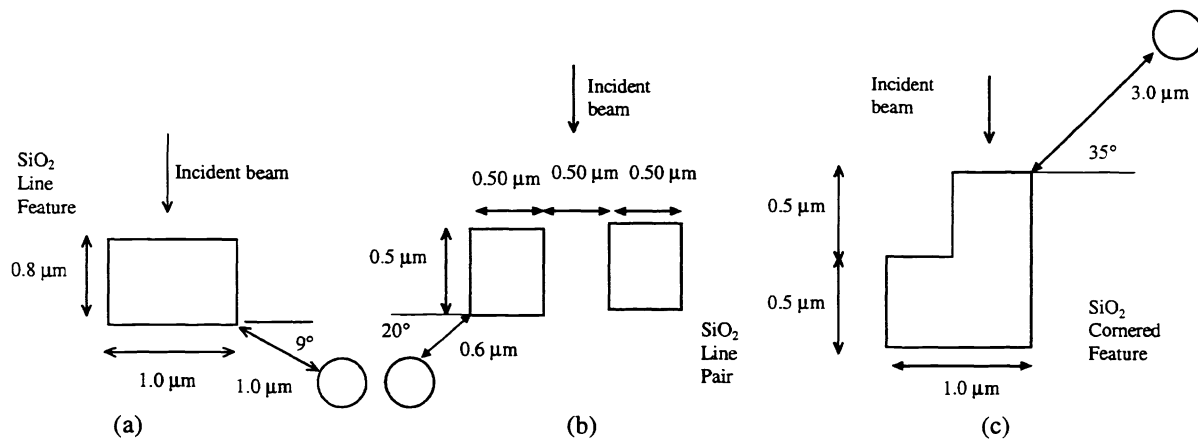
Figure 1. Overhead view of the geometric configuration for the SiO₂ features and PSL contaminants considered (a) line feature, (b) line pair, (c) cornered feature. The diameters of the contaminating spheres are 0.482 μm and the patterned features are approximately 0.27 μm thick.

The sizes of the features were determined by an atomic force microscope at Arizona State University and the approximate positions of the spheres were determined using an optical microscope. Comparisons are made between numerical scattering predictions by DDSURF and experiments conducted at ASU.

We will first discuss the coupled-dipole method used to model the features. Next, we will briefly discuss the experimental procedure taken to measure the scattering from the features, and then comparisons between numerical predictions and experimental results will be presented.

2. COUPLED-DIPOLE METHOD

2.1 Background

The first models developed to predict scattering from spherical features used Lorenz-Mie based formulation. However, it is impossible to find perfectly spherical features or contaminants in industry. The method used here, called the coupled-dipole method was first developed to model scattering from features in free space. Modifications to the method have been made to include features on surfaces. The coupled-dipole method uses an array of dipoles to model the electromagnetic characteristics of scattering features. An electrical field applied to a dipole induces a dipole moment. As will be shown, the dipole moment can be determined from the dipole equations. Once the dipole moment field within a feature is determined, the scattered field outside the feature can be determined.

2.2 Coupled-Dipole Method

We will now consider the development of the coupled-dipole method. Figure 2 shows an example of a dipole arrangement used to model a feature on a surface. The feature-particle arrangement in Fig. 2 corresponds to the geometric configuration found in Fig. 1a.
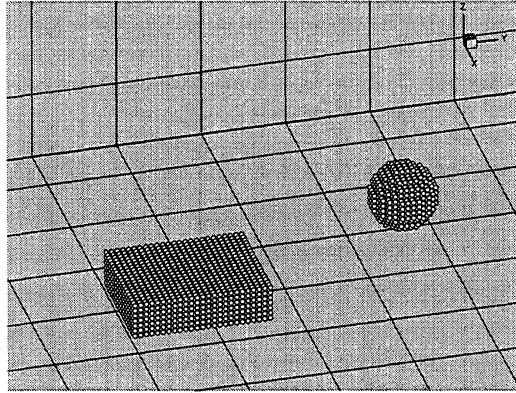
Figure 2. Example of dipole configuration for a rectangular feature with a spherical particle contaminant on a surface.

The field within the features can be determined by a set of equations relating the dipole moment to the total electric field at each dipole. Simultaneous solving for each dipole in the lattice is necessary, as each dipole simultaneously affects the electric field with each other. We will first consider the local dipole equations, and then extend these equations into matrix equations for to solve for each dipole.

2.1 Local equations

A dipole moment is induced when an electric field is present at a dipole i. The dipole moment, $\overline{P}_i$, is related to the total electric field present, $\overline{E}_{tot,i}$, by the dipole polarizability α_i:

$$\overline{P}_i = \alpha_i \overline{E}_{tot,i}.$$ (1)

Several models for the polarizability have been developed and are discussed by Draine and Goodman.[6] DDSURF has the flexibility to use various models, but we have utilized the recommended lattice dispersion relation which enables an array of dipoles with finite lattice spacing to emulate a continuum.

Referring to Figure 3, the total electric field at the dipole, $\overline{E}_{tot,i}$ is the summation of the contributions from the field from the incident beam, the field present due to direct interaction between the dipoles, and the dipole fields due to reflection from the surface:

$$\overline{E}_{tot,i} = \overline{E}_{inc,i} + \overline{E}_{direct,i} + \overline{E}_{reflected,i}.$$ (2)
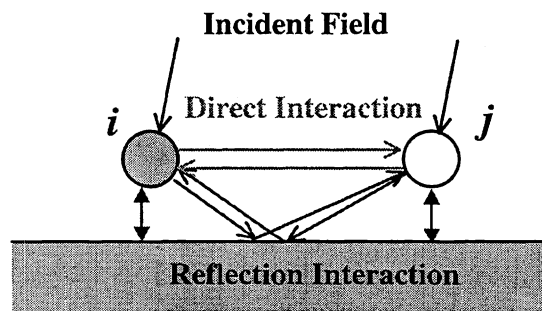

Figure 3. Modes of interaction between dipoles above a surface.

Substituting Eq. (2) into Eq. (1) we obtain an equation in terms of the three components of the total field:

$$\left(\alpha_i\right)^{-1}\overline{P}_i - \overline{E}_{direct,i} - \overline{E}_{reflected,i} = \overline{E}_{inc,i}.$$ (3)

The electric field by direct interaction between a dipole and every other dipole can be found with the summation relating the dyadic Green's function to the dipole moment:[5]

$$\overline{E}_{direct,i} = \frac{k_0^2}{\varepsilon_0}\sum_{j\neq i}\overline{G}_{ij}\cdot\overline{P}_j.$$ (4)

The electric field interaction between dipoles due to reflection from the surface, $\overline{E}_{reflected,i}$, can be represented as[5]

$$\overline{E}_{reflected,i} = \sum_{j=1}^{N}\left(\overline{S}_{ij} + \frac{k_2^2}{\varepsilon_0}\frac{k_1^2 - k_2^2}{k_1^2 + k_2^2}\overline{G}_{ij}^I\right)\cdot\overline{P}_j.$$ (5)

The Sommerfeld integral terms, $\overline{S}_{ij}$, are computed numerically using routines developed by Lager and Lytle,[7] where k_1 and k_2 are the wave numbers for the particle and the surface respectively, and ε_0 is the permittivity.

2.2 Global equations

Since the state of each dipole is affected by all other dipoles, the local equations for each dipole must be solved simultaneously, thus a matrix equation is used. The matrix equation for the entire problem can be represented as

$$(\overline{B} + \overline{A} + \overline{R})\overline{P} = \overline{E}_{inc}.$$ (7)

For N total dipoles, $\overline{B}$ is the diagonal matrix of the inverse of the polarizabilities:

$$\overline{B} = diag(\alpha_{1x}^{-1}, \alpha_{1y}^{-1}, \alpha_{1z}^{-1}, \cdots, \alpha_{Nx}^{-1}, \alpha_{Ny}^{-1}, \alpha_{Nz}^{-1},),$$ (8)

and $\overline{A}$ is the matrix that corresponds to Eq. (4) which is for direct interaction and $\overline{R}$ is the matrix that corresponds to Eq. (5) for the reflected field interaction.

2.3 Solution of the matrix equations

The dipole spacing used to model a feature should be small compared to the electric field wavelength within the feature. For this criterion to be satisfied, the relation $|m|kd \leq \beta$ should hold true for reasonable accuracy, where d is the dipole lattice spacing, m is the refractive index, k is the wave number, and β is a number of the order of unity.[3] Thus, for a feature of a particular material there is a maximum lattice spacing. The number of dipoles needed for accurate modeling increases with increasing feature size and/or refractive index. For the cases considered here, the features were of made of material of SiO$_2$ ($m=1.46$) and PSL ($m=1.59$), and the common dipole spacing used were of the order of 0.03 μm.

For our applications, a large number of dipoles (>1000) to model the features is often required. Direct matrix methods such as LU decomposition would require $O(N^3)$ operations, thus it can prove to be inefficient for large numbers of dipoles. Iterative methods, such as the complex conjugate gradient (CCG) method, can be used to solve the matrix equations. DDSURF uses the CCG algorithm developed by Petravic and Kuo-Petravic[8] and used by Draine.[2] To reduce the number of mathematical operations needed to $O(N\log N)$ from $O(N^2)$, a two-dimensional FFT was introduced.[5]

2.4 Far zone approximation

In order to find the scattering pattern at the detector region, we need to determine the electric field in the far zone. A post processor called RDSURF was developed to compute the far field from the dipole moment distribution within the particle. From the particle to the receiving detector, there are two scattering components to consider. One component is by direct scattering from each dipole, and the other component is that which reaches the detector after reflection off the surface. The latter component is found using the Fresnel equations.
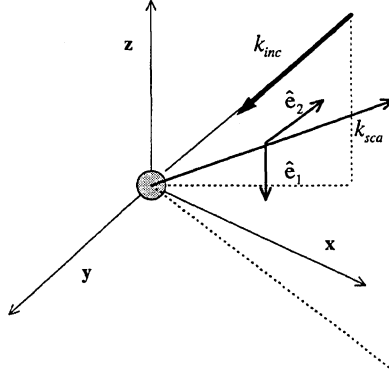
Figure 4. Geometrical configuration for far field scattering.

By summing contributions from each dipole with the far-zone approximation, with the geometry based on Fig. 4, we get

$$\overline{E}_{sca}(r) = k_0^2 \frac{\exp(ik_0 r)}{4\pi r} \sum_{j=1}^{N} \left\{ \begin{array}{l} \exp(-ik_{sca}r_j)\left[(\overline{P}_j \cdot e_1)e_1 + (\overline{P}_j \cdot e_2)e_2 \right] + \\ \exp(-ik_{sca}r_j)\left[R^{TM}(\overline{P}_j \cdot e_1)e_1 + R^{TE}(\overline{P}_j \cdot e_2)e_2 \right] \end{array} \right\}, \tag{11}$$

where R^{TM} and R^{TE} are the Fresnel reflection coefficients. The far-field irradiance can be found by multiplying the scattered electric field by its complex conjugate:

$$I_{sca}(r) = \overline{E}_{sca}(r)\overline{E}_{sca}^{\Psi}(r). \tag{12}$$

2.5 Computed parameters

At Arizona State University, experimental results for scattering from the particles on surfaces are collected in the form of differential scattering cross-section, $dC_{sca} / d\Omega$. The differential scattering cross-section is defined as the energy scattered per unit time into a unit solid angle about a certain direction. Bohren and Huffman[9] derived an expression for this:

$$\frac{dC_{sca}}{d\Omega} = \lim_{\Omega \to 0} \left(\frac{C_{sca}}{\Omega} \right) \approx \frac{I_{sca}(r)A}{I_{inc}(A / r^2)} = \frac{r^2 I_{sca}(r)}{I_{inc}}, \tag{13}$$

where $I_{sca}(r)$ is the scattered irradiance, A is the detection area, r is the distance from the feature to the point of detection, I_{inc} is the incident irradiance, and Ω is the detection solid angle.

3. EXPERIMENT

Experiments for comparison with numerical results were conducted at ASU by Greg Starr. The ASU scatterometer uses a helium-neon laser beam ($\lambda = 632.8$ nm) to create the scattering signature from the feature on a surface. The scattered light from the feature on the surface is detected by a ring/wedge photodetector.[10] The ring/wedge detector consists of 32 rings and 32 wedges which act as individual detectors. The detector is centered on the specular, and for all cases considered here the incident angle (θ_i) is 45° from the surface normal, and the distance from the feature to the detector center is 8.2 mm. Figure 5a shows the configuration of the detector with respect to the wafer surface and feature and Fig. 5b shows the configuration of the rings and wedges on the detector.
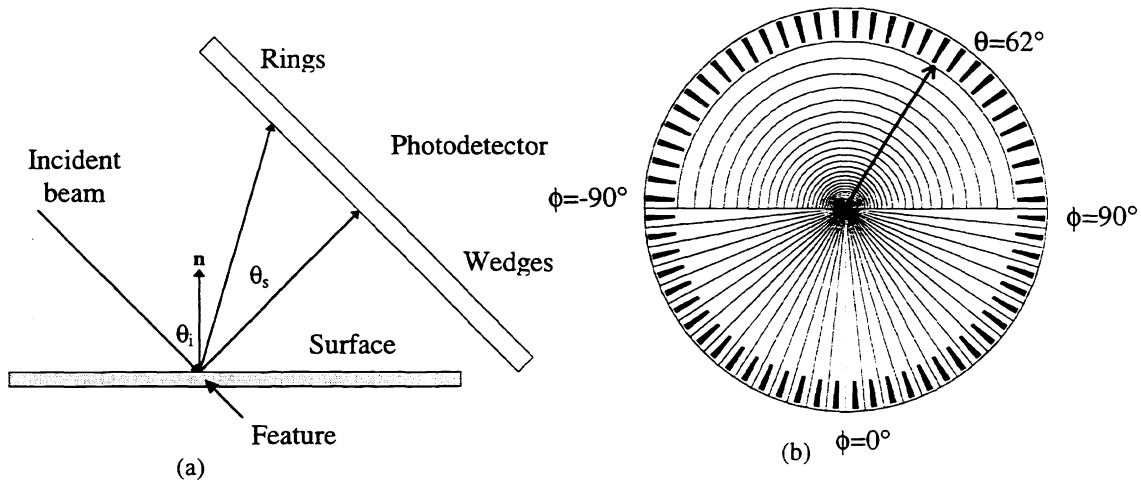
Figure 5. Example of ring/wedge photodetector configuration with respect to feature location.

Experimentally, the differential scattering cross-section is determined at each ring. Each ring is a photodetector, and the resulting calibrated voltage is converted into $dC_{sca} / d\Omega$. Bawolek[10] presents the method used to convert from voltage to $dC_{sca} / d\Omega$. Numerically, the post-processor RDSURF calculates the differential scattering cross-section at discrete points on the detector geometry. To model the ringed areas, RDSURF averages the $dC_{sca} / d\Omega$ computed at the discrete points that lie within each individual detector.

4. RESULTS AND DISCUSSION

In this work we investigate the effect of patterned wafer particle contamination on the light scattering signature and compare experimental scattering measurements to model predictions by DDSURF. We will first show the scattered light irradiance distribution on the plane of detection as predicted by DDSURF. To determine the accuracy of DDSURF and quantify the scattering signature, comparisons between experimentally determined and numerically predicted differential scattering cross-sections are made for several different configurations found on the patterned wafer standard die.

4.1 Scattering from Contaminant Only

First we will present the scattering pattern from a 0.482 μm diameter PSL sphere on a Si surface. Figure 6a displays the geometric configuration of the plane surface where the ring/wedge photodetector lies with respect to the illuminated feature. Figure 6b shows the scattered irradiance distribution from the isolated sphere for an s polarized incident beam.
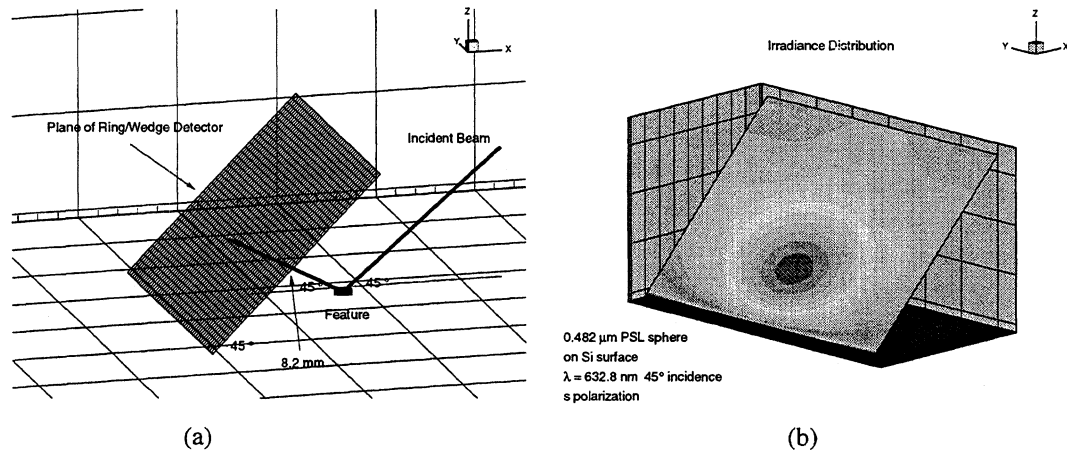
(a)

(b)

Figure 6. (a) Geometric configuration of plane of detection with respect to scattering feature. (b) Irradiance distribution along plane of detection from a 0.482 μm PSL sphere.

The scattering can be quantified by comparison of the differential scattering cross-section found experimentally and determined numerically. Figure 7a shows the predicted and experimentally determined differential scattering cross-sections found over varying angle of the ringed region of the ring/wedge detector. Figure 7b shows the comparisons for the wedge region of the detector found experimentally and numerically. We see that the numerical predictions correspond well with the experimental measurements. The error bars on the experimental values are a 3 sigma distribution of the results found by repeating the experiments 5 times.

(a)

(b)
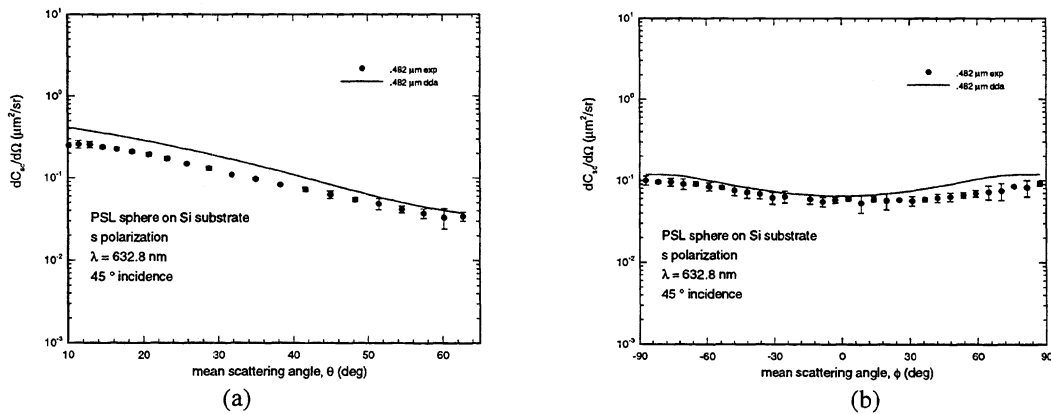
Figure 7. Differential scattering cross-section found experimentally and by DDSURF for 0.482 μm PSL sphere on silicon surface at the (a) ringed region, and (b) wedge region.

4.2 Scattering from Patterned Features with Contaminants

We will now consider the effect that a spherical contaminant particle will have on the scattering from the geometric features shown in Fig. 1.

4.2a Irradiance Distribution

Figures 8 through 10 shows the numerically determined irradiance distribution along the detector plane for the three patterned features shown in Figure 1. Figures 8a, 9a, and 10a show the scattered irradiance from the features when no

contaminating particle is present, while Figs. 8b, 9b, and 10b show the scattered irradiance when a contaminating particle is present.
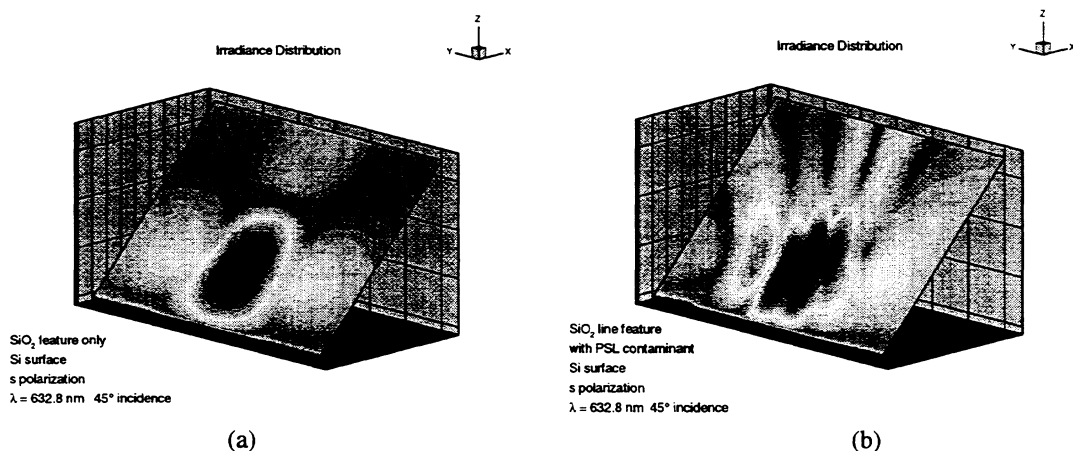

(a)

(b)

Figure 8. Irradiance distribution on detector plane for SiO₂ line: (a) feature only, (b) feature with contaminating 0.482 μm PSL sphere on silicon surface. The geometrical configuration of the feature and particle corresponds to Fig. 1a.
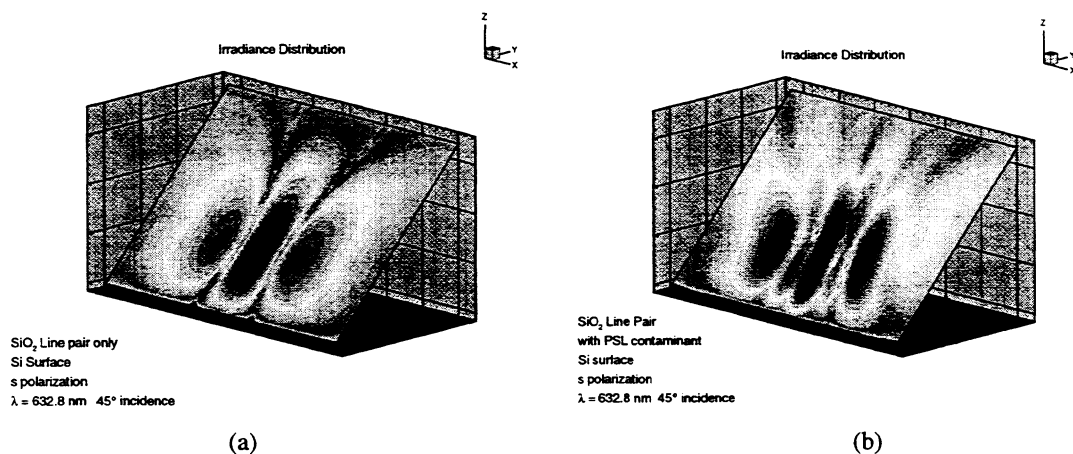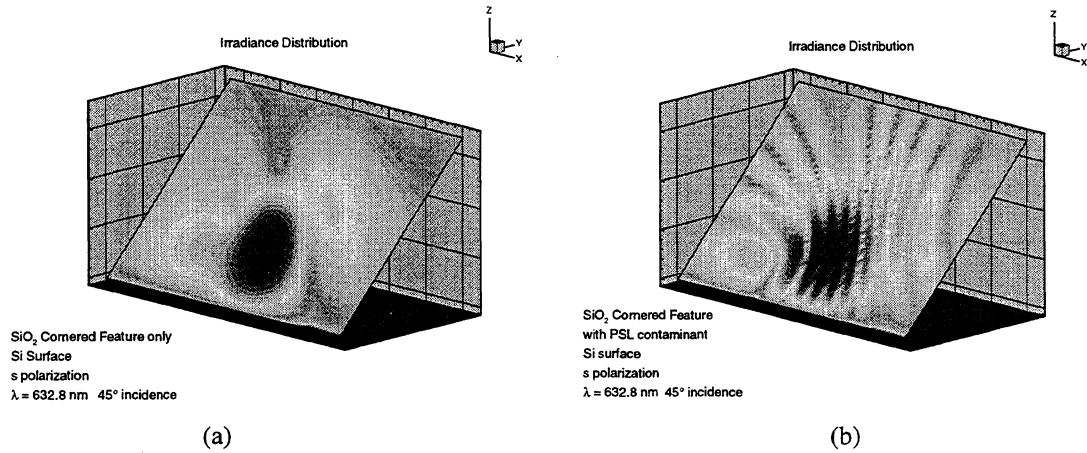

(a)

(b)

Figure 9. Irradiance distribution on detector plane for SiO₂ line pair: (a) features only, (b) features with contaminating 0.482 μm PSL sphere on silicon surface. The geometrical configuration of the feature and particle corresponds to Fig. 1b.

Figure 10. Irradiance distribution on detector plane for SiO_2 cornered feature: (a) feature only, (b) feature with contaminating 0.482 µm PSL sphere on silicon surface. The geometrical configuration of the feature and particle corresponds to Fig. 1c.

4.2b Differential Scattering Cross-Section

To quantify the scattering data, and to compare numerical predictions to experimental measurements, we find the differential scattering cross-section, $dC_{sc}/d\Omega$, for each ring and wedge photodetector in the ASU ring/wedge detector. RDSURF modeled the detector so that direct comparisons could be made with experiment. The differential scattering cross-section angular variation provides different information between the ring data and the wedge data. Feature size information can be obtained from the $dC_{sc}/d\Omega$ variation from the ring data, while shape features such as the symmetry of a feature or position of particle contaminants can be obtained from the wedge data.

4.2b.1 Ring Data

Figures 11a, 12a, and 13a show the ring data for the differential scattering cross-section for the line feature, line pair feature, and cornered feature respectively as shown in Fig. 1 when no contaminant is present. Figures 11b, 12b, and 13b are the corresponding differential scattering cross-sections when a contaminating particle is introduced. Good agreement is found between the experimental results and the numerical predictions. We see that introduction of a particle contaminant does not increase in the difference between experimental and numerical results. Agreement between experiment and DDSURF is found to be closer for the cases with the particle contaminant.
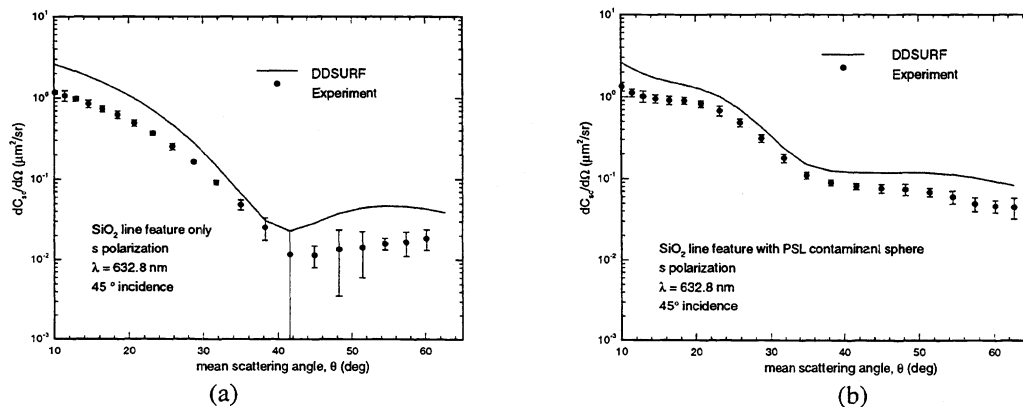

Figure 11. $dC_{sca}/d\Omega$ angular variation in ring region for SiO_2 line: (a) feature only, (b) feature with 0.482 µm PSL contaminant sphere on a silicon surface. The geometrical configuration of the feature and particle corresponds to Fig. 1a.
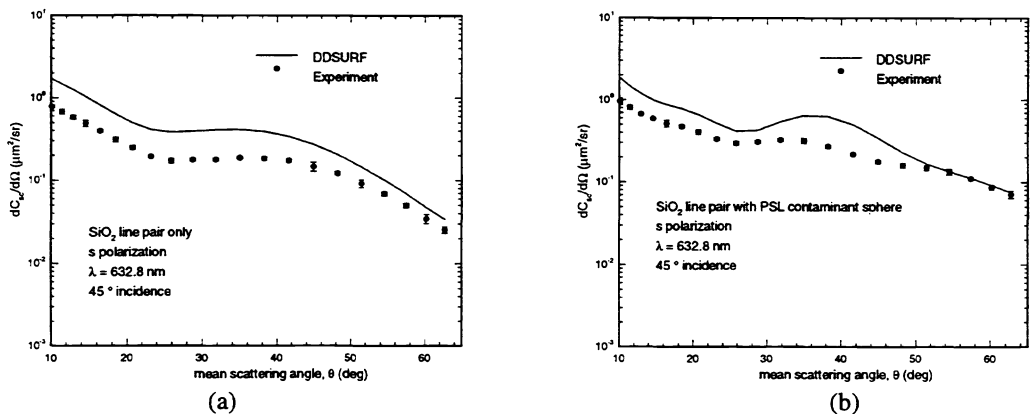
Figure 12. $dC_{sca}/d\Omega$ angular variation in ring region for SiO_2 line pair: (a) features only, (b) features with 0.482 μm PSL contaminant sphere on a silicon surface. The geometrical configuration of the feature and particle corresponds to Fig. 1b.
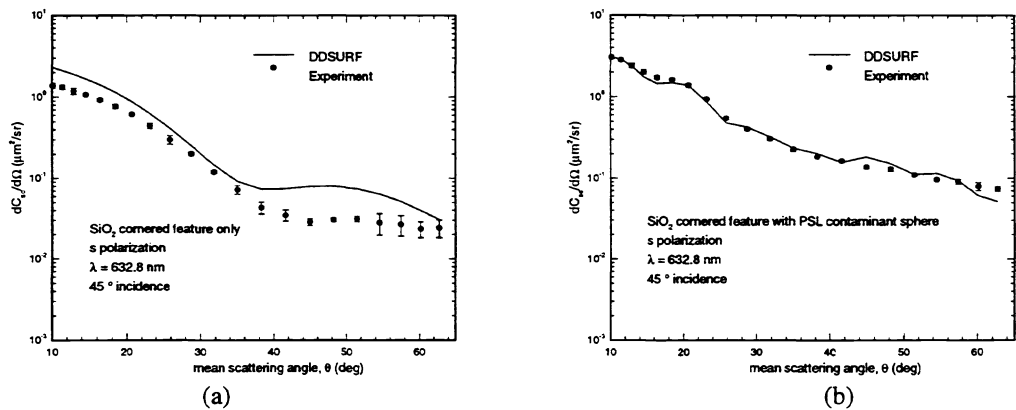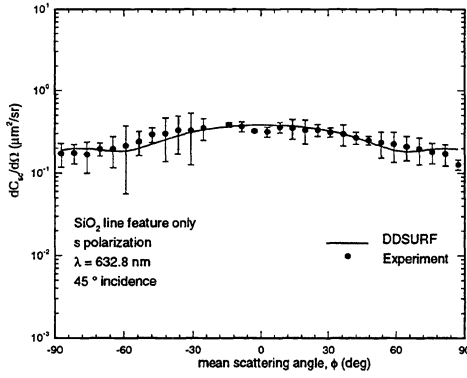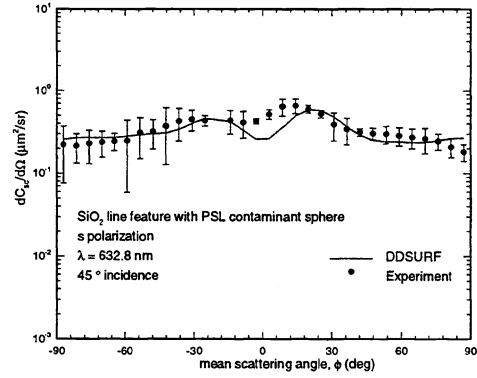

Figure 13. $dC_{sca}/d\Omega$ angular variation in ring region for SiO_2 cornered feature: (a) feature only, (b) feature with 0.482 μm PSL contaminant sphere on a silicon surface. The geometrical configuration of the feature and particle corresponds to Fig. 1c.

4.2b.2 Wedge Data

    Figures 14a, 15a, and 16a show the wedge data for the differential scattering cross-section for the line feature, line pair feature, and cornered feature respectively as shown in Fig. 1 when no contaminant is present. Figures 14b, 15b, and 16b show the corresponding differential scattering cross-sections when a contaminating particle is introduced. As found with the ring data in Figs. 11-13, good agreement is found between the experimental results and the numerical predictions by DDSURF. Most of the results here are very close to, or lie within, the experimental error. Introduction of the particle contaminant has a significant effect on the $dC_{sca}/d\Omega$ variation in the wedge data. We notice the introduction of a bump in the data due to scattering from the contaminant. This bump would change position with variation of the contaminant position.
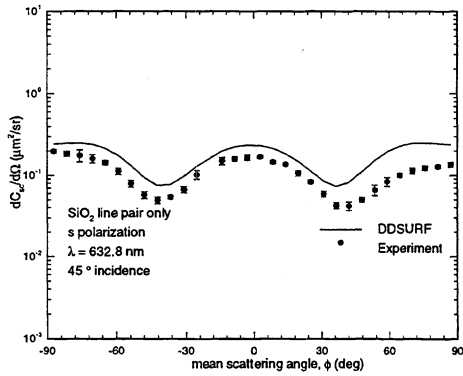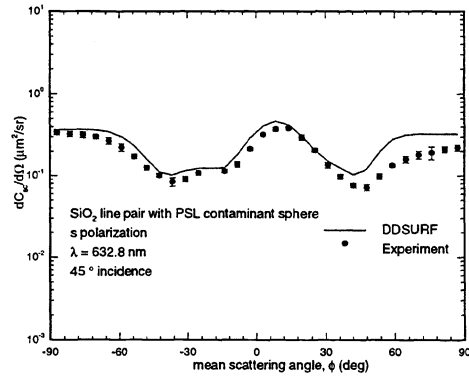
Figure 14. $dC_{sca}/d\Omega$ angular variation in wedge region for SiO_2 line: (a) feature only, (b) feature with 0.482 μm PSL contaminant sphere on a silicon surface. The geometrical configuration of the feature and particle corresponds to Fig. 1a.

Figure 15. $dC_{sca}/d\Omega$ angular variation in wedge region for SiO_2 line pair: (a) features only, (b) Features with 0.482 μm PSL contaminant sphere on a silicon surface. The geometrical configuration of the feature and particle corresponds to Fig. 1b.

Figure 16. $dC_{sca}/d\Omega$ angular variation in wedge region for SiO₂ cornered feature: (a) feature only, (b) feature with 0.482 μm PSL contaminant sphere on a silicon surface. The geometrical configuration of the feature and particle corresponds to Fig. 1c.
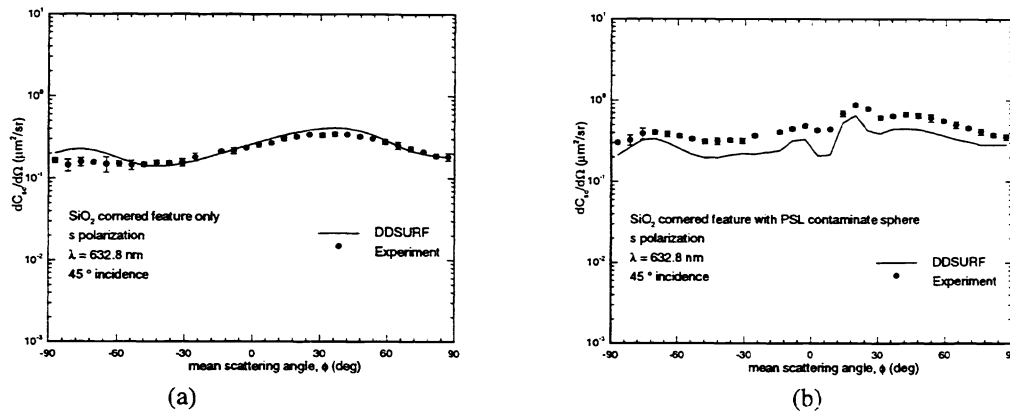
5. CONCLUSIONS

Particle contamination can be detected by evaluation of light scattering from patterned wafers. We have shown comparisons between experiment and the numerical model DDSURF. The predictions by DDSURF agreed well with the experimentally determined differential scattering cross-section. The method shows promise as a flexible predictive method for scattering characteristics that could be used with surface scanning inspection systems.

6. ACKNOWLEDGMENTS

7. REFERENCES

1. E. M. Purcell and C. R. Pennypacker, "Scattering and Absorption of Light by Nonspherical Dielectric Grain," *Astrophysical Journal*, Vol. 186, pp. 705-714, 1973.

2. B. T. Draine, "The Discrete-Dipole Approximation and its Application to Interstellar Graphite Grains," *Astrophysical Journal*, Vol. 333, pp. 848-872, 1988.

3. B. T. Draine and P. J. Flatau, "The Discrete-Dipole Approximation for Scattering Calculations," *J. Opt. Soc. Am. A*, Vol. 11, pp. 1491-1499, 1994.

4. M. A. Taubenblatt and T. K. Tran, "Calculation of Light Scattering from Particles and Structure by the Coupled-Dipole Method," *J. Opt. Soc. Am. A*, Vol. 10, pp. 912-919, 1993.

5. R. Schmehl, "The Coupled-Dipole Method for Light Scattering for Light Particles on Plane Surfaces," (Department of Mechanical and Aerospace Engineering, Arizona State University and Institut für Thermische Strömungsmaschinen, Universität Karlsruhe, Germany, 1994).

6. B. T. Draine and J. Goodman, "Beyond Clausius-Mossotti: Wave Propagation on a Polarizable Point Lattice and the Discrete Dipole Approximation," *Astrophysical Journal*, Vol. 405, pp. 685-697, 1993.

7. D. L. Lager and R. J. Lytle, *Fortran Subroutines for the Numerical Evaluation of Sommerfeld Integrals unter Anterem*, Rep. UCRL-51821, Lawrence Livermore Laboratory, Livermore, Calif., 1975.

8. M. Petravic and G. Kuo-Petravic, "An ILUCG Algorithm Which Minimizes in the Euclidean Norm," *Journal of Computational Physics*, Vol. 32, pp. 263-269, 1979.

9. C. F. Bohren and D. R. Huffman, *Absorption and Scattering of Light by Small Particles*, (John Wiley and Sons, 1983).

10. E. J. Bawolek, "Light Scattering by Spherical Particles on Semiconductor Surfaces," PhD Dissertation, Arizona State University, Dept. of Mechanical and Aerospace Engineering, 1992.